nature communications

Article

https://doi.org/10.1038/s41467-025-65630-1

Electrochemical potential-driven water dynamics control CO_2 electroreduction at the Ag/H_2O interface

Received: 18 June 2025

Accepted: 20 October 2025

Published online: 27 November 2025

Check for updates

Xiongwei Tian[1,2], Axel Tosello Gardini[2,3], Umberto Raucci[2], Hai Xiao[4] ✉, Yuqun Zhuo[1,5] ✉ & Michele Parrinello[2] ✉

A molecular-level understanding of the catalyst-electrolyte interface under realistic operating conditions remains a central challenge in electrocatalysis. In particular, the role of the electrochemical potential in modulating interfacial solvation, and its consequences for CO_2 electroreduction, has yet to be fully elucidated. Here, using machine learning-accelerated molecular dynamics simulations, an explicit solvent model within the grand canonical DFT framework, and enhanced sampling techniques, we systematically investigate the impact of the working potentials on CO_2 reduction process at the $Ag(111)/H_2O$ interface. Our results reveal that the applied potential significantly reshapes the orientation of interfacial water and modulate the strength of hydrogen-bond network. This collective solvent response to the electric potential plays an important role in stabilizing reactive intermediates, regulating reaction kinetics, and facilitating key steps such as proton transfer and hydroxide diffusion. These findings underscore the critical role of solvent dynamics in CO_2 reduction, highlighting the importance of simulating electrochemical reactions under realistic operating conditions. Rather than acting as a passive background medium, the solvent emerges as a dynamic, potential-sensitive participant that plays an active role in the catalytic process.

The electrochemical reduction of CO_2 has emerged as a critical technology in a clean energy economy, holding the promise of mitigating carbon emission and producing value-added feedstock such as carbon monoxide, formic acid, and hydrocarbons[1–5]. The reduction of CO_2 typically occurs at the catalyst-electrolyte interface, where the interplay of the applied potential, ionic composition, pH, and solvent controls the catalytic process[6,7]. Among the various factors, it is assumed that the electric potential plays a pivotal role in CO_2 reduction[8,9]. As illustrated in Fig. 1, in a typical CO_2 reduction system, an external constant potential is applied to the cathode, causing negative charge accumulation on the surface of the catalyst[7]. The electric field formed at the catalyst-electrolyte interface alters the spatial distribution of ions and solvent molecules near the surface and directly influences the reaction mechanism[10,11].

Traditionally, theoretical models have treated the applied potential primarily through its direct electrostatic effects, such as stabilizing charged intermediates or modulating adsorption energies[12–14]. However, in this framework, the water solvent is generally treated as a passive background medium, overlooking its role within the electrochemical interface[10]. In fact, the applied potential alters the orientation, hydrogen bonding, and dynamics of interfacial water and, thus, has a direct impact on reactivity[15–19]. Despite substantial progress in understanding electrochemical mechanisms, a complete atomistic picture of the electrochemical interface under

[1]Key Laboratory for Thermal Science and Power Engineering of Ministry of Education, Department of Energy and Power Engineering, Tsinghua University, Beijing, China. [2]Atomistic Simulations, Italian Institute of Technology, Genoa, Italy. [3]Department of Materials Science, Università di Milano-Bicocca, Milan, Italy. [4]Department of Chemistry, Tsinghua University, Beijing, China. [5]Shanxi Research Institute for Clean Energy, Tsinghua University, Taiyuan, China. ✉e-mail: haixiao@tsinghua.edu.cn; zhuoyq@tsinghua.edu.cn; michele.parrinello@iit.it

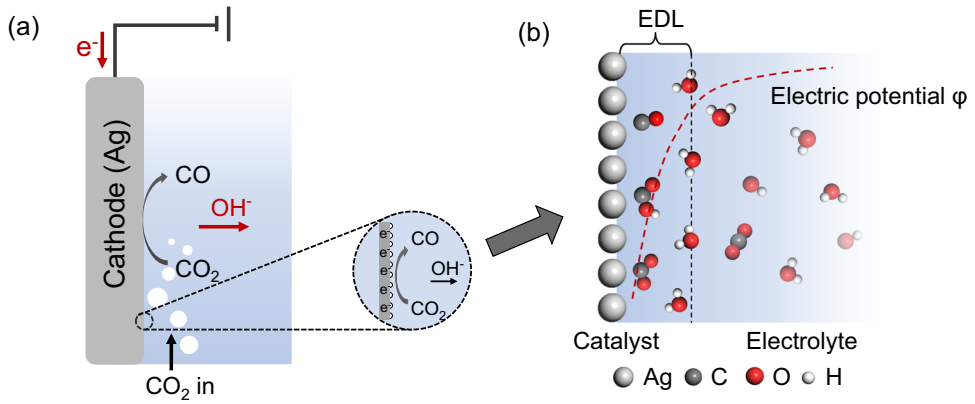

Fig. 1 | Representation of the electrochemical interface for CO_2 reduction. a Scheme of the cathode side of an H-type cell for CO_2 reduction. **b** Scheme of the microscopic electrified catalyst-electrolyte interface for CO_2 reduction.

working conditions remains elusive and represents a significant computational challenge.

Capturing the subtle interplay between applied potential and interfacial water dynamics requires simulations that combine electronic accuracy with extended sampling under constant-potential conditions[9]. Ab initio molecular dynamics (AIMD) simulations have provided important insights into interfacial chemistry, but the simulated timescales are limited by their high computational costs and the difficulty of controlling the electrode potential. To mimic the effect of an applied potential during the reaction, one common approach involves introducing alkali metal cations near the interface[16,18,20]. However, the resulting electric bias tends to fluctuate as the reaction progresses, deviating from the conditions of a truly constant-potential experiment. Alternatively, constant-potential conditions can be modeled by combining grand-canonical ensemble DFT (GCE-DFT) with implicit solvent models, allowing the total number of electrons to change in response to the target potential[21,22]. This approach avoids the need for explicit solvent molecules and maintains computational efficiency, but it still lacks the ability to capture specific solvent-solute interactions and interfacial solvent dynamics[8,12]. More recently, hybrid explicit-implicit solvent models have been developed within the framework of GCE-DFT to better capture interfacial solvent structure while maintaining constant-potential conditions[23,24]. However, updating the electron count at each self-consistent field step makes these simulations even more computationally demanding than standard AIMD[25]. As a result, the high cost of explicit ab initio methods continues to limit simulation timescale and system sizes, hindering an accurate modeling of the coupled influence of the electric potential and solvent dynamics on CO_2 electroreduction[7,9].

To address these limitations, machine learning interatomic potentials (MLIPs) have recently emerged as a powerful tool for modeling reactive systems with near DFT accuracy and significantly extended the scope of these simulation[26–28]. When combined with enhanced sampling techniques[29], MLIP-driven simulations allow for the systematic exploration of complex reaction pathways[30–33], solvent-mediated dynamics[34], and rare events that are otherwise inaccessible to conventional methods[35,36].

In the context of electrochemical systems, these methodologies have been successfully applied to characterize interfacial water and to investigate the kinetics of key reactions such as oxygen reduction[37], hydrogen evolution[38–40], and formic acid decomposition[41]. However, most existing studies remain limited to zero-charge conditions, which do not reflect the constant-potential environments that govern real electrocatalytic processes.

In this work, we combined state-of-the-art machine learning-accelerated molecular dynamics simulations, explicit solvent model within the GCE-DFT framework to perform constant-potential simulations, and enhanced sampling methods to investigate the CO_2 electroreduction mechanism on the Ag(111) surface. We chose silver as the model catalyst due to its well-established selectivity and industrial prospect for the CO_2-to-CO conversion[42]. Silver exhibits a high CO Faraday efficiency that exceeds 90% and supports current densities above 200 mA/cm^2, making it a benchmark system for both fundamental studies and practical applications[2,3]. We considered two electrochemical potentials: the potential of zero charge (PZC) and a constant potential (CP) corresponding to experimentally relevant working conditions. By constructing two MLIPs, each trained to reproduce DFT-level energies and forces under PZC and CP conditions, we unraveled the full complexity of the CO_2 reduction process under operando electrochemical conditions. Our simulations reveal that the applied potential affects reaction barriers not simply through electronic effects, but through the dynamic reorganization of the solvent environment, which governs the accessibility and stability of reactive intermediates and transition states. This coupling especially influences the hydrogenation step and the corresponding ion-pair dissociation process, whose barriers and kinetics are particularly influenced by the solvent response to the electric bias.

Results

As anticipated in the Introduction, we compare the results under two distinct electrochemical potential conditions: the potential of zero charge (PZC) and a constant potential (CP) of −1.5 V vs. SHE. The latter closely approximates the experimental onset potential for CO_2 reduction on Ag[43,44], while PZC represents a key reference state where no excess charge is present on the surface[45]. This comparison provides insight into how the solvent environment and reaction kinetics respond to the applied potentials. To capture the differences between these conditions, we trained two separate sets of MLIPs to model the Ag(111)/H_2O interface and the CO_2-to-CO reaction pathway under PZC and CP, respectively. A detailed description of the MLIP training workflow is provided in the "Methods" section and illustrated in Supplementary Fig. 1.

Ag(111)/H_2O interface response to the applied potential

We first explore the response of the interfacial water structure and dynamics to the applied working potential. As shown in Fig. 2a and b, the applied potential has a significant impact on the structure of the interfacial water. At PZC condition, the O density profile (Fig. 2a, upper) exhibits two distinct peaks at 2.7 Å and 3.2 Å from the Ag surface, corresponding to two close adsorption layers of water oxygen atoms. The distribution of water dipole orientation reveals a peak at ~55° in Fig. 2b, and the angle distribution between one O–H bond of water and surface normal (z-direction) shows a peak at ~80° (Supplementary Fig. 3), indicating that the interfacial water molecules

https://doi.org/10.1038/s41467-025-65630-1

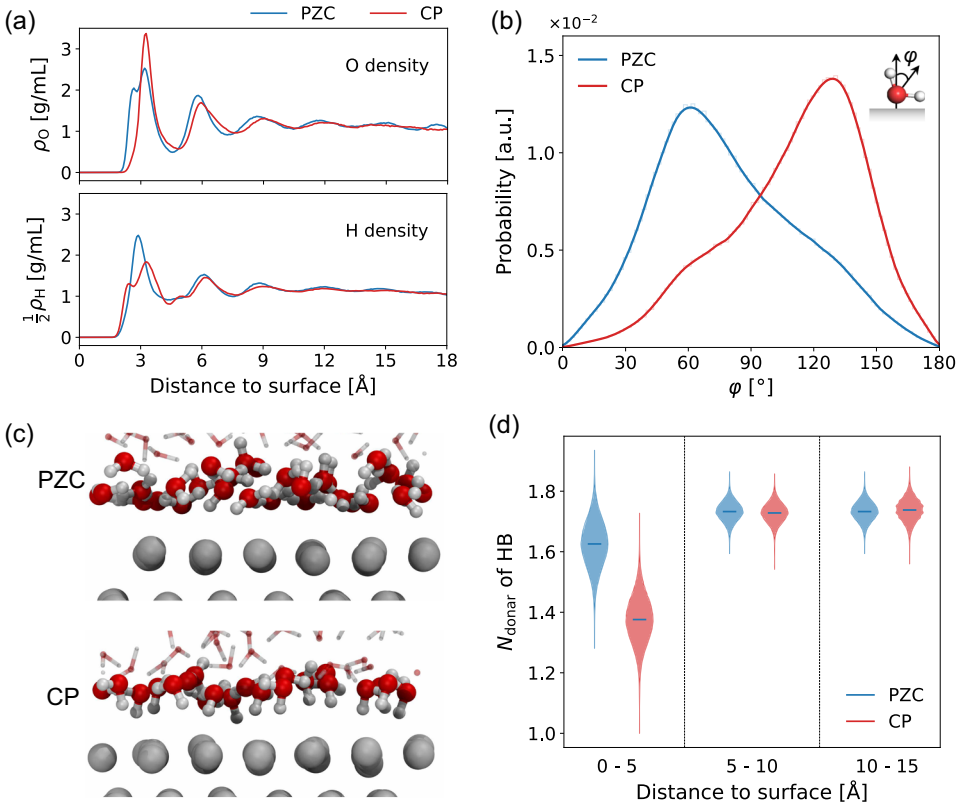

Fig. 2 | Characterizations of Ag(111)/H_2O interface at PZC and CP conditions. **a** Oxygen (upper) and hydrogen (lower) density profiles of water along the surface normal (*z*-direction), where the zero corresponds to the location of the Ag surface. **b** Probability distribution of the angle φ between the bisector of the water H–O–H angle and the *z*-direction computed for the interfacial water molecules (φ is shown in the inset). The interfacial water is taken as being within 5 Å from the Ag surface, as suggested in the density profiles in (**a**). **c** Representative snapshots of Ag(111)/H_2O interface at PZC and CP conditions. The Ag, O, and H atoms are colored in light gray, red, and white, respectively, while the water molecules outside the interfacial region are displayed in transparent stick style for clear illustration. **d** Violin plot showing the distribution of the averaged hydrogen-bond donor number of water in the interfacial region (0–5 Å), intermediate region (5–10 Å), and bulk region (10–15 Å). The blue horizontal lines represent the mean value of N_{donor}. All results were obtained from unbiased trajectories of a 6 × 6 Ag(111) slab with 180 water molecules (Supplementary Fig. 2a and Supplementary Table 1), for a total simulation time of 2.5 ns.

slightly tilt toward the electrolyte, with one O–H bond nearly parallel to the Ag surface at PZC condition.

However, when a negative potential is applied to the interface, the peak in the O density profile at 2.7 Å disappears, while two peaks could be observed in the H-density profile close to the Ag surface (Fig. 2a, down). The dipole orientation of water has a peak at ~135°, and the distribution of the angle between one O–H bond of water and the surface normal shows two peaks at around 100° and 155°. These results suggest that the interfacial water molecules rotate to a "H-down" structure due to the electrostatic attraction between the negatively charged Ag substrate (Supplementary Fig. 4) and the positively charged H atoms of water molecules (see Fig. 2c, and the Supplementary Video 3). Additional features appear in the density profile at approximately 6 Å and 9 Å. These peaks indicate the presence of partially ordered water layers. Beyond this region, the density gradually approaches 1 g/cm^3 under both potential conditions, consistent with the bulk-like water behavior. The two-dimensional distribution of water dipole along the *z*-direction (Supplementary Fig. 5) confirms that the influence of electric potential on water is confined to the interface and gradually diminishes as one moves away from it.

In addition to the static structural properties of water near the interface, it is essential to investigate its dynamic behavior under the two electrochemical conditions. Following the water density profile along *z*, we identify three different regions: interfacial (0–5 Å), intermediate (5–10 Å), and bulk (10–15 Å). The averaged number of hydrogen-bond donors of water molecules (N_{donor}) in these regions is shown as a violin plot in Fig. 2d. The mean value of N_{donor} within the interfacial region decreases from 1.62 to 1.38 as the potential shifts from PZC to CP conditions. This is consistent with the "H-down" structure of interfacial water at CP conditions, where some H atoms orient toward and interact directly with the Ag surface, rather than participating in hydrogen bonding with neighboring water molecules. The distribution of the N_{donor} is nearly identical across the intermediate and bulk water regions. Moreover, we observed a slight enhancement in the mobility of interfacial water under CP conditions, as evidenced by a broader distribution of displacement vectors (Supplementary Fig. 6). Further analysis indicates that the hydrogen-bond lifetime of interfacial water at CP conditions is 21.2% shorter than at PZC (Supplementary Fig. 7). Additionally, both the libration and H–O–H bending modes exhibit a noticeable red shift (Supplementary Fig. 8), indicating a weaker hydrogen-bond environment near the electrified Ag surface[16,46,47].

The distinct properties of interfacial water at negative potential are consistent with previous studies on Pt/H_2O and Au/H_2O interfaces, investigated via in situ Raman spectroscopy and AIMD simulations[15,16,48]. These findings validate the reliability of our MLIPs in modeling the behavior of the Ag(111)/H_2O interface under varying potential conditions and provide a solid foundation for further exploration of CO_2 reduction reactions at the Ag(111)/H_2O interface.

CO_2 adsorption process

The CO_2 reduction to CO is widely recognized to proceed through four elementary steps[49,50]: (1) CO_2 adsorption, (2) $^*CO_2$ hydrogenation

https://doi.org/10.1038/s41467-025-65630-1

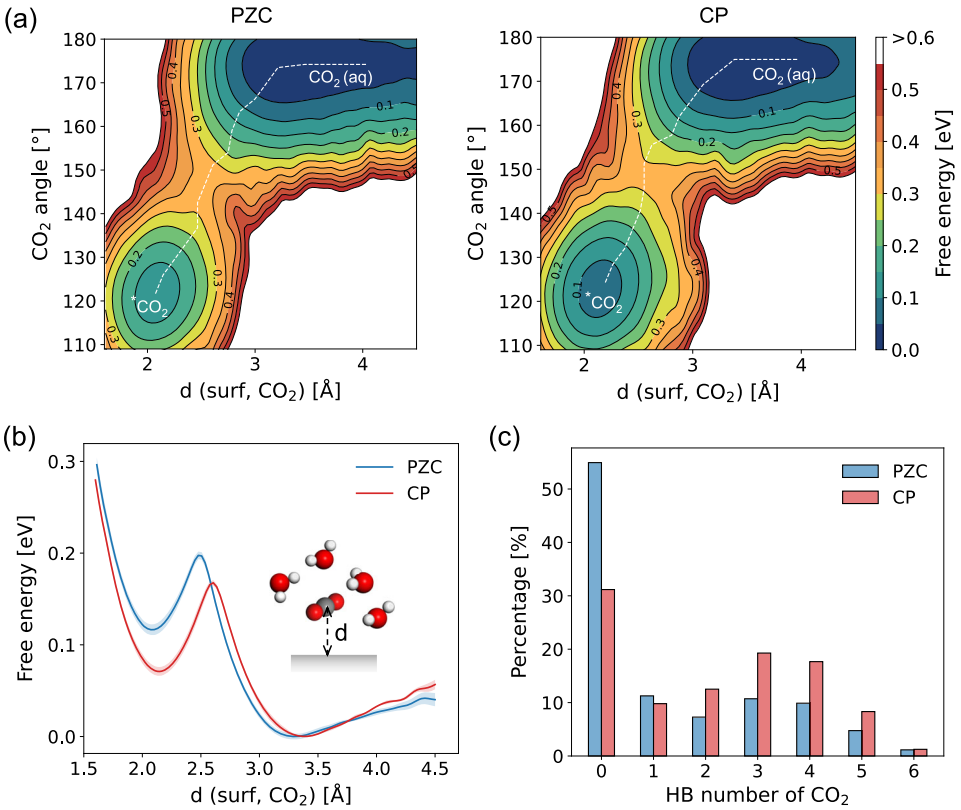

Fig. 3 | Potential-dependent energetics and solvation structure in CO_2 adsorption process. a Two-dimensional FES as a function of the vertical distance of CO_2 from the surface (d) and O=C=O angle of CO_2 at PZC (left) and CP (right) conditions. The minimum free energy pathway from CO_2(aq) to $^*CO_2$ is depicted with a white dashed line, and it is computed using the MEPSA (Minimum Energy Path Surface Analysis) package[79]. **b** One-dimensional projection of the FES along the vertical distance of CO_2 from the surface, the statistical errors are calculated using the weighted-block average techniques as discussed in ref. 77 and displayed with shaded colors in the plot. In the inset, the Ag slab is shown in light gray, C in dark gray, O in red, and H in white. **c** Histogram showing the distribution of the number of hydrogen bonds formed with CO_2 during the intermediate stage of the CO_2 adsorption process (2.25 Å < d < 2.75 Å).

leading to the formation of *COOH, (3) splitting of this intermediate, followed by (4) the final *CO desorption (Supplementary Table 2). Here, we adopt a step-by-step strategy to systematically investigate how the potential-driven changes in interfacial water structure and dynamics regulate the above steps of CO_2R.

We first analyzed the CO_2 absorption process, and converged the free energy surface as a function of the z-distance (d) of CO_2 from the surface and the O=C=O bond angle (Fig. 3a), using the on-the-fly probability enhanced sampling (OPES) method[29] (See "Methods" and Supplementary Table 3). Two metastable states were identified, both in the absence and in the presence of the applied potential: a solvated CO_2 state in which the solute is to be found at the interfacial region (CO_2(aq)) and one in which it is chemisorbed ($^*CO_2$). The shape of the FES is very similar in the two scenarios. The CO_2 molecule, which is linear in the solvated phase, bends to an angle of approximately 115–130° upon adsorption. The equilibrium distance between the $^*CO_2$ center of mass and the surface is approximately 2.1 Å.

The FESs projected along the distance d from the surface are shown in Fig. 3b. The adsorption energy is 0.13 eV and 0.08 eV at PZC and CP conditions, respectively. The enhanced stability of $^*CO_2$ can be attributed to the increased surface charge density at CP (Supplementary Fig. 4), which facilitates charge transfer from the surface to the adsorbed CO_2, as confirmed by the Bader charge analysis in Supplementary Fig. 9[50]. The effect of the electric bias is to decrease the barrier for adsorption from 0.20 eV at PZC to 0.16 eV at CP and shift slightly the transition state (TS) position from d = 2.45 Å to d = 2.6 Å. This TS stabilization is likely due to its increased solvation at CP compared to the PZC condition, since in the CP state, the free hydrogen atoms in the first H-density peak (~2.7 Å) could effectively form a hydrogen bond with CO_2. In contrast, under PZC conditions, the water structure is more rigid, thereby hindering interfacial water reorientation and CO_2 solvation. This is reflected in the histogram shown in Fig. 3c, where we observe a decrease in the percentage of configurations with zero hydrogen bonds and an increase in those where CO_2 is solvated by three or more water molecules under CP conditions (Supplementary Fig. 10).

Furthermore, to investigate the influence of the electrochemical potential on the dynamics of $^*CO_2$, we performed 1 ns unbiased molecular dynamics simulations under both PZC and CP conditions. The $^*CO_2$ adopts a bidentate structure and adsorbs near the top-site of the Ag surface. One C–O bond aligns parallel to the surface and coordinates with two sites, while the other C–O bond tilts toward the electrolyte (Supplementary Fig. 11). The $^*CO_2$ can rotate, alternatively aligning its C–O bonds with the surface, and this behavior occurs more frequently under CP conditions (Supplementary Fig. 12 and Supplementary Video 2). Furthermore, the $^*CO_2$ molecule exhibits large diffusion at CP, exploring a wide range of adsorption sites, whereas it remains largely confined to a few sites under PZC conditions (Supplementary Fig. 13). Interestingly, this dynamic behavior does not significantly affect the C–O bond length, which shows minimal variation upon coordination with the Ag surface, fluctuating around 1.26 Å (Supplementary Fig. 14).

Our results differ significantly from those reported in previous studies based on implicit solvent models[13,51]. The most remarkable difference is that, in the implicit solvent framework, CO_2 does not chemisorb on the surface under PZC conditions, as indicated by a

https://doi.org/10.1038/s41467-025-65630-1

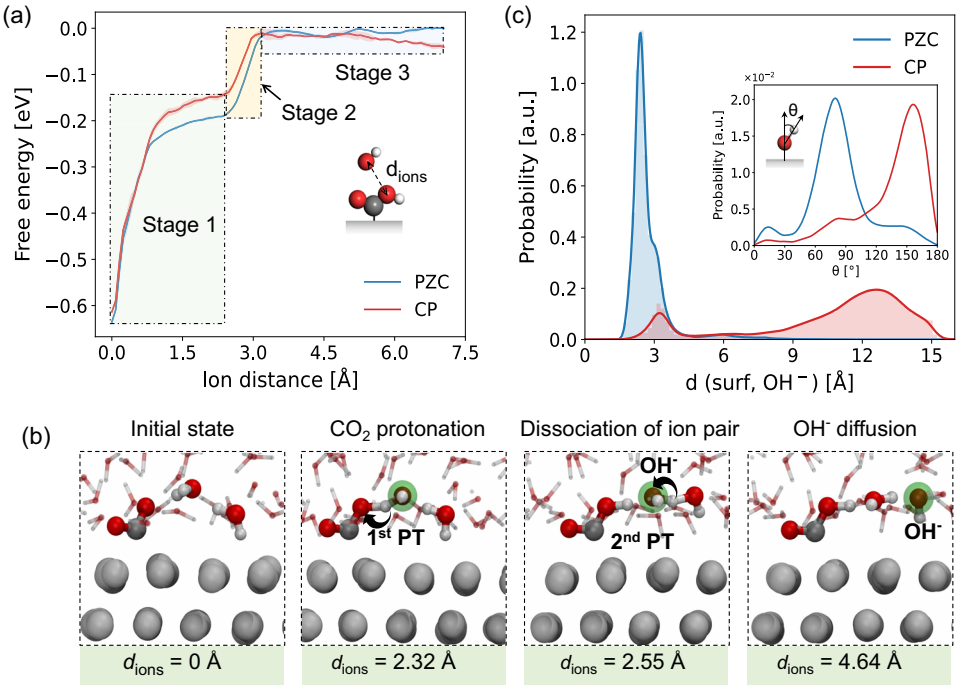

Fig. 4 | Influence of potential on $^*CO_2$ hydrogenation process. a One-dimensional projection of the FES along the distance of ions (*COOH and OH^-), with three distinct stages identified: CO_2 protonation (Stage 1), dissociation of the ion-pair of *COOH and OH^- (Stage 2), and OH^- diffusion (Stage 3). The endpoint of stage 2 is used as the reference point to align the free energy curves to allow a direct comparison of the free energy of OH^- diffusion under two potential conditions. In the inset, the Ag slab is shown in light gray, C in dark gray, O in red, and H in white. **b** Representative snapshots illustrating three stages of $^*CO_2$ hydrogenation process, captured from the biased trajectory at CP condition. The colors in the snapshots represent Ag in light gray, C in dark gray, O in red, and H in white. Only the water molecules involved in the reaction are shown in ball-and-stick style, while others are displayed in transparent stick style for clear illustration. The green transparent ball illustrates the location of hydroxyl or OH^-. **c** Probability distribution of the vertical distance between OH^- and the surface from 10 independent unbiased trajectories of OH^- diffusion. The inset shows the probability distribution of OH^- orientation when the ion stays within the interfacial region (with a vertical distance less than 5 Å).

positive adsorption free energy. Moreover, the influence of the applied potential on the free energy profile is much more pronounced in the implicit solvent case, with marked shifts observed as the potential is varied from PZC to negative potentials. We further investigated this effect by training MLIP models at different applied potentials using an implicit solvent environment, as detailed in Supplementary Notes 1 and 2 and Supplementary Figs. 15 and 16, recovering the literature results.

Our findings suggest that the inclusion of explicit solvent in our simulations plays a key role in moderating the effect of the applied potential. The explicit solvent environment appears to partially screen the electric field at the interface, thereby reducing the potential-induced shifts in the free energy during CO_2 adsorption. This comparison underscores the crucial role of solvent representation in electrochemical modeling and highlights the necessity of incorporating explicit solvent to accurately capture interfacial molecular interactions and reaction mechanisms.

$^*CO_2$ hydrogenation step

The adsorption of CO_2 involves an electron transfer from the metal surface to the molecule, leading to a slightly negative intermediate. Bond analysis of $^*CO_2$ in Supplementary Fig. 14 indicates that this intermediate is not sufficiently activated for C–O bond cleavage, necessitating its hydrogenation as a critical step toward CO formation. To investigate the hydrogenation of $^*CO_2$, we designed two collective variables (CVs): the first CV is the coordination number between the oxygen atoms of CO_2 and the hydrogen atoms of all water molecules [C.N. (O_{cd}, H_w)], which is able to describe the proton transfer from H_2O to $^*CO_2$. The second CV is the ion-pair distance (d_{ions}) between *COOH and OH^-, which accounts for the formation of the stable intermediate. The resulting free energy profile projected along the ion-pair distance is shown in Fig. 4a, while representative snapshots are shown in Fig. 4b and Supplementary Video 3. The reaction proceeds via three different stages, as reflected in the FES profile. The first one involves the proton transfer from one water molecule to $^*CO_2$, leading to the formation of *COOH and OH^- ion pair (first proton transfer, 1st PT). However, this ion pair is initially tightly bound, exhibiting a strong tendency to recombine and return to the reactant state. To stabilize the protonated product, the *COOH–OH pair must dissociate. This occurs through the diffusion of OH^- away from *COOH (stage 2, 2nd PT), facilitated by the Grotthuss mechanism, consistent with previous reports[50,52]. Once the distance between *COOH and OH^- exceeds 3.2 Å, the free energy profile reaches a plateau (stage 3).

An interesting feature emerges in the stage 3 region of the free energy profile, where the free energy remains nearly constant with increasing ion-pair distance under PZC conditions, but gradually decreases beyond ~5 Å under CP condition. This subtle difference is also reflected in the two-dimensional FES (Supplementary Fig. 17). To explore the origin of this behavior, we analyzed the distribution of CV values during the OPES simulations. At PZC, the *z*-distance distribution between OH^- and surface reveals that the hydroxide ion remains confined near the surface, whereas under CP condition, it can diffuse more freely into the bulk (Supplementary Fig. 18). To further analyze the effect of the negative potential on OH^- dynamics, we carried out 10 independent unbiased molecular dynamics simulations under PZC and CP conditions, respectively. Each trajectory was initialized with a single OH^- ion positioned above the surface and run for 1 ns. The statistical distribution of the *z*-distance between OH^- and the surface is shown in Fig. 4c. At PZC, the OH^- ion remains tightly bound to the electrode, diffusing primarily within the interfacial region. In

https://doi.org/10.1038/s41467-025-65630-1

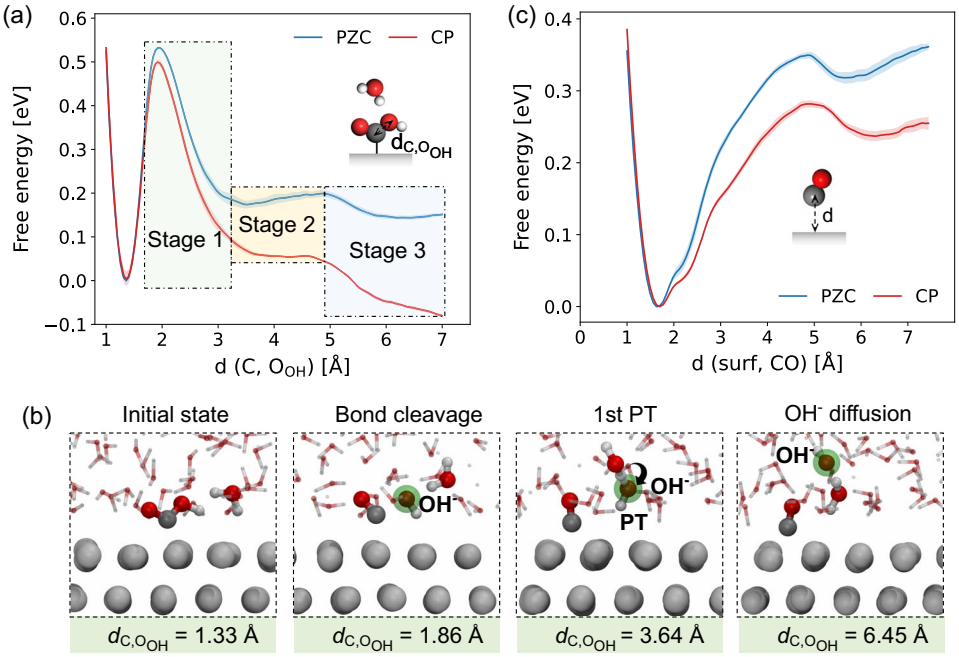

Fig. 5 | *COOH splitting and CO desorption processes. a One-dimensional FES of *COOH splitting along the distance between the C atom and the O atom of the hydroxyl/hydroxide group, with three stages identified: bond cleavage (Stage 1), first proton transfer of OH^- (Stage 2), and OH^- diffusion (Stage 3). **b** Representative snapshots illustrating three stages of the *COOH splitting process, captured from the biased trajectory at CP condition. The colors in the snapshots represent Ag in light gray, C in dark gray, O in red, and H in white. The green transparent ball illustrates the location of OH^-. Only the water molecules involved in the reaction are shown in ball-stick style, while others are depicted in transparent stick style for clear illustration. **c** One-dimensional FES of the CO desorption process along the vertical distance of CO from the surface. The reference minima of the free energy profiles are aligned to the initial states in both FES plots for better comparison of the free energy difference at PZC and CP conditions. In the inset, the Ag slab is shown in light gray, C in dark gray, O in red, and H in white.

contrast, under the CP condition, it rapidly desorbs from the surface and diffuses into the bulk region (Supplementary Fig. 19 and corresponding Supplementary Video 4). This analysis highlights the strong influence of electrochemical conditions on OH^- dynamics. Under negative potentials, lower than PZC, the OH^- ion is electrostatically repelled from the electrode, whereas at PZC, its diffusion is hindered. Additionally, the orientation of OH^- near the interface exhibits distinct behavior under these two potential conditions (inset of Fig. 4b). Under the CP condition, OH^- tends to adopt a vertical orientation, with the O–H bond pointing toward the surface. In contrast, at PZC, the ion predominantly adopts a horizontal configuration, lying flat on the electrode surface while remaining confined to the interfacial region. The freedom of OH^- to diffuse away from the electrode results from the weakening of the hydrogen-bond network in the interfacial region at CP, where the interfacial water molecules reorient such that one hydrogen atom points toward the electrode, facilitating its diffusion via the Grotthus mechanism. Together, these effects promote OH^- diffusion into the bulk and contribute to the lower free energy barrier for ion-pair dissociation observed in stage 2. This change in diffusion also explains the energy trend in stage 3: restricted OH^- motion at PZC leads to a nearly constant free energy, while bulk diffusion at CP results in a gradual decrease of the free energy.

*COOH splitting mechanism

Before proceeding to describe the last electrochemical step that leads to the formation of *CO, we replaced the OH^- formed in the previous step by one water molecule to simulate the neutralization effect of the buffer solution under experimental conditions[50] (the influence of interfacial pH on *COOH splitting is discussed in Supplementary Note 3, Supplementary Table 4 and Supplementary Fig. 20).

Once electrolyte neutrality is re-established, the *COOH intermediate remains stably adsorbed on the surface under both PZC and CP conditions. Furthermore, the length of the protonated C–O bond in *COOH is slightly longer under CP compared to PZC (Supplementary Fig. 21). This bond elongation suggests greater activation of the C–O bond for cleavage under the effect of the applied potential.

The free energy profile for the *COOH dissociation process as a function of the C–O distance ($d_{C,O_{OH}}$) is shown in Fig. 5a. Three distinct stages can also be observed here, and these are: C–O bond cleavage (stage 1), first proton transfer (1st PT, stage 2), and OH^- diffusion (stage 3) (Fig. 5b and Supplementary Video 5). The transition state appears at a $d_{C,O_{OH}}$ of 1.94 Å under both potential conditions, with similar activation energies (0.53 eV at PZC and 0.49 at CP, respectively). As observed in the $^*CO_2$ hydrogenation step, the free energy profile gradually decreases under CP conditions as the $d_{C,O_{OH}}$ distance increases beyond ~5 Å, while it remains nearly flat at PZC. This behavior can be explained similarly to the $^*CO_2$–to–*COOH hydrogenation case, considering the distinct OH^- dynamics at PZC and CP. Indeed, also here, the formed OH^- remains surface-bound at PZC, whereas under CP condition, it tends to diffuse into the bulk electrolyte, contributing to the observed decrease in free energy (Supplementary Fig. 22).

From a mechanistic point of view, our simulations suggest that the cleavage of the C–OH bond in *COOH is not initiated by protonation of the hydroxyl group (Supplementary Fig. 23). Instead, the bond breaks first, resulting in the formation of an OH^- species, which subsequently migrates away from the surface via the Grotthuss mechanism. This sequential bond cleavage, followed by proton transfer, contrasts with the mechanism proposed in previous studies based on the computational hydrogen electrode (CHE) model[53,54], where this step is typically treated as a concerted proton-coupled electron transfer process.

*CO desorption process

As the final step, we have investigated the desorption of *CO. The *z*-distance between the carbon atom of CO and the surface is selected as the CV to obtain the FES of the desorption process, and

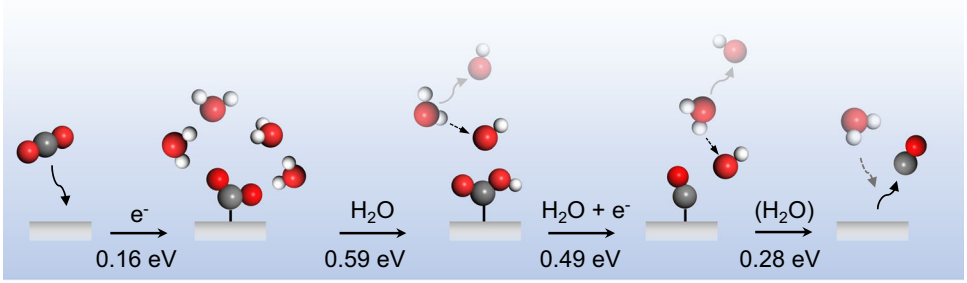

Fig. 6 | Mechanism of CO_2 reduction to CO. Schematic illustration of the proposed reaction pathway for CO_2 reduction in a neutral electrolyte under electrochemical working potentials. The free energy barrier of each elementary reaction step at an applied potential of −1.5 V vs. SHE is shown below the corresponding arrow. The free energy barriers ($\Delta G^{\ddagger}$ and free energy differences ΔG) of each elementary step are listed in Supplementary Tables 5 and 6. In the schematic, the slab is shown in light gray, C in dark gray, O in red, and H in white.

the resulting free energy surface is shown in Fig. 5c. The equilibrium position of the *CO lies at approximately 1.7 Å from the surface, sitting in the first layer of interfacial water. As shown in Supplementary Fig. 24, *CO primarily binds to the hollow site of the second Ag layer, but migrates through multiple adsorption sites under both potential conditions. Similar to the behavior of $^*CO_2$, *CO exhibits larger mobility under CP conditions, sampling nearly all surface sites within 1 ns.

The FES reveals that the barrier for CO desorption is 0.07 eV lower under CP conditions compared to PZC. Interestingly, the TS is located approximately 5 Å above the surface, which corresponds to the thickness of the interfacial solvent layer. Bader charge analysis indicates that the net charge of *CO is nearly identical in both potential conditions, with the adsorbed molecule being slightly negatively charged (Supplementary Fig. 25). At CP the electrostatic repulsion between the negatively charged surface and *CO may weaken the M–C bonding interaction, making the *CO desorption primarily controlled by the interfacial hydrogen-bond disruption and solvent reorganization. The desorption process requires the breaking of the interfacial hydrogen-bond network and releases a surface adsorption site, which is subsequently reoccupied by a nearby water molecule[55] (Supplementary Fig. 26). At CP, the weakened hydrogen-bond network facilitates both the migration of CO through the interfacial region and the rapid reorganization of water molecules to refill the adsorption site. These two effects collectively contribute to lowering the desorption barrier under CP conditions.

Therefore, although CO desorption is typically considered a nonelectrochemical process, our results indicate that it is indirectly influenced by the applied potential. The negative potential weakens the hydrogen-bond network within the interfacial water layer, facilitating the desorption of CO molecules. This promotes the continuation of subsequent CO_2 reduction, ensuring the sustainable catalytic performance of the system.

Discussion

The schematic mechanism for the overall CO_2 electroreduction to CO under working electrochemical conditions is shown in Fig. 6. Our simulations identify the hydrogenation of $^*CO_2$ as the rate-determining step, with a free energy barrier of 0.59 eV at −1.5 V vs. SHE. Crucially, this barrier is not simply dictated by the direct electrostatic stabilization induced by the applied potential, but is strongly modulated by the electric-bias-driven reorganization of the interfacial water network. Prior studies often underestimated this barrier by overlooking the dissociation dynamics of the *COOH–OH^- ion pair. Our enhanced sampling-based approach captures this dissociation as a distinct, water-mediated step controlled by proton transfer and solvent structure, refining the mechanistic picture of CO_2 reduction.

Indeed, a central insight from our work is that the electric bias reshapes interfacial water structure and dynamics, which in turn governs key reaction steps. Under negative potential, water molecules adopt a "H-down" orientation and form a weakened hydrogen-bond network. This disruption reduces the rigidity of interfacial water, enhancing solvation flexibility and facilitating proton transfer and OH^- diffusion via the Grotthuss mechanism. These solvent-mediated effects are not secondary, as OH^- diffusion plays a critical role across multiple steps and is highly sensitive to interfacial water structure. At PZC, OH^- remains confined near the surface, whereas under negative potential, it diffuses into the bulk, stabilizing intermediates and contributing to the overall free energy landscape. Even CO desorption, traditionally seen as a nonelectrochemical event, is indirectly modulated by the interfacial solvent. The weaker hydrogen-bond network at negative potential lowers the energetic barrier for CO to escape into the electrolyte. Thus, even non-redox steps become field-sensitive through water-mediated effects.

This broader understanding of the reaction mechanism also challenges once more the traditional idea that catalytic activity depends only on specific sites on the surface[30,31,56]. The active catalytic environment should instead be seen as the coupled system of the electrode and the interfacial water layer. Moreover, these are not purely local effects confined to the adsorption site, but they reflect a nonlocal, collective response of the interfacial layer to the electric potential. As such, the catalytic performance emerges from global electric bias-induced restructuring of the electrode-electrolyte microenvironment, rather than arising purely from local adsorption interactions at the surface.

Our results underscore the need to treat solvents explicitly and dynamically, and they establish machine learning-accelerated molecular dynamics coupled with enhanced sampling techniques as a powerful framework for capturing the complexity of electrochemical interfaces. Looking ahead, tuning this interfacial environment offers a promising route to enhance CO_2 reduction kinetics. In practical systems, alkali metal cations (Na^+, K^+, Cs^+, etc.) play a crucial role at the electrode-electrolyte interface by promoting surface charge accumulation, modulating the interfacial electric field, and stabilizing key reactive intermediates[49,57,58]. While explicit cation effects were not included in the present simulations, their strong coupling to electrochemical potential-driven water dynamics makes a systematic investigation of their role under working conditions a promising direction for future studies, and our computational framework is readily extendable to incorporate these effects.

Methods

DFT single-point calculations

The Ag(111)/H_2O interface was modeled using 5-layer p(3 × 3) and 4-layer p(4 × 4) Ag(111) slabs, with 30 and 58 water molecules placed above the Ag surface, respectively, corresponding to a density of 1 g/cm^3. All DFT energy and force calculations were performed with Vienna Ab initio Simulation Package (VASP)[59,60], where the projector

augmented wave (PAW) pseudopotentials were used[61,62]. The electron exchange-correlation potential was described using r^{2}SCAN functional[63], with rVV10 correction applied to account for the nonlocal van der Waals interactions[64]. The kinetic energy cutoff for the plane wave basis expansion was set to 500 eV. The first-order Methfessel–Paxton scheme with a smearing width of 0.2 eV was used. The convergence threshold for self-consistency was set to 1×10^{-6} eV. The Brillouin zone was sampled using a k-point grid of $3 \times 3 \times 1$ and $2 \times 2 \times 1$ for p(3×3) and p(4×4) slab models, respectively. A 15 Å vacuum layer was perpendicularly added to the model to eliminate the spurious interactions between periodic images (Supplementary Table 1).

The self-consistent implicit solvation model implemented in VASPsol[21,65] was employed in the region of vacuum layer, with the aim to calculate the electric potential (U) by referencing the Fermi level (E_{Fermi}) of the system against the standard hydrogen electrode (SHE):

$$U(\text{ v.s. SHE}) = -\frac{E_{Fermi}}{e} - U_{SHE} \quad (1)$$

where U_{SHE} is the absolute electrode potential of SHE, with a fitted value of 4.21 V in this work (Supplementary Method 1 and Supplementary Fig. 27). In VASPsol, the relative permittivity of the solvent was set to 78.4 to represent water, and the Debye length was set to 3.04 Å, corresponding to a bulk electrolyte concentration of 1 M. A SOLHYBRID model[24] was patched to the original VASPsol to avoid the possible nonphysical interaction of implicit solvation with explicit water molecules (Supplementary Fig. 28). This hybrid explicit/implicit solvent model (illustrated in Supplementary Fig. 1a) has been validated for computing electrode potential and performing GCE-DFT calculations[23,24,66,67].

Two types of DFT calculations were performed to calculate the energies and forces of configurations under PZC and CP conditions (Supplementary Fig. 1c). At PZC, the number of valence electrons ($N_{e,PZC}$) was used, corresponding to the conventional constant-charge DFT calculations (Supplementary Fig. 29). In contrast, under CP conditions, the number of electrons (N_e) of each configuration was externally optimized to reach the preset constant electric potential with a convergence threshold of 0.01 V, which is denoted as GCE-DFT. The optimization of N_e was implemented with a fully-converged constant-potential (FCP) algorithm in ref. 25. The potential-dependent electronic grand-canonical free energy of the system under CP condition was calculated as

$$\Omega_{el}(U) = E(U) - (N_e - N_{e,PZC}) \cdot E_{Fermi} \quad (2)$$

where $E(U)$ is the electronic energy under the applied potential.

Machine learning interatomic potentials

Two sets of MLIP were constructed for describing CO_2 reduction reaction at the Ag(111)/H_2O interface under PZC and CP (−1.5 V vs. SHE) conditions, respectively. Fitting separate MLIPs for a grand-canonical potential energy surface at a desired electric potential is a practical strategy, since electrochemical reactions proceed at the electronic ground state in an open system[25]. Nevertheless, looking ahead, developing an MLIP capable of modeling electrocatalytic processes across a continuous range of potentials is highly desirable. Recent studies by Liu et al. and Zhou et al. have made promising progress toward this direction[68,69], introducing approaches that predict the Fermi level from the atomic configuration and the number of electrons, and dynamically adjust the electron count during the MD simulations to maintain the target desired potential.

In this work, each MLIP was trained using MACE version 0.3.4[28], one of the state-of-the-art graph neural networking (GNN) architectures, which combines equivalent message passing with a high body-order description of the local atomic environment via spherical harmonic polynomials, leading to excellent performance in accurate modeling of complex atomic interactions while maintaining efficiency[70]. Each model was trained with 128 equivariant messages and 2 interaction layers. A cutoff of 6 Å was employed. The dataset was split into training/validation subsets with a ratio of 95:5, with a batch size of 5 for training and 10 for validation. A weighted loss function was employed with force and energy weights set to 1000 and 10, respectively. The training process was carried out with 350 epochs, with the last 20% of epochs switching to the Stochastic Weight Averaging strategies to lower the energy errors. Four different MLIP models were trained to estimate model uncertainty using a query-by-committee approach.

Active learning procedure

The initial configurations of the training set were collected from MD simulations with the MACE-MP-0[71,72], a pre-trained MLIP model that covers 89 elements on 1.6 M bulk crystals in the MPTrj dataset. The model has been proven to reasonably describe the behavior of solid-liquid interfaces[70]. We then applied an active learning protocol to generate new configurations through MD simulations with MLIPs that have been built during training. Specifically, we evaluated the maximum standard deviation of the atomic forces predicted by the committee of four different MLIP models in each electric potential scenario[30] ($\sigma = \max_i \sqrt{\frac{1}{4}\sum_{\alpha=1}^{4} \left\| F_i^{\alpha} - \overline{F_i} \right\|^2}$). Training configurations were selected according to their associated σ values, following a strategy similar to that adopted in refs. 30,73.

Even with the availability of MLIPs, numerous reactive processes, such as complex chemical reactions, typically occur on timescales far exceeding those accessible by performing standard MD simulations. This limitation makes it prohibitive to thoroughly sample a broad spectrum of reactive species across all possible reaction pathways. To this effect, we combined the protocol with enhanced sampling methods to ensure a comprehensive exploration of the reaction landscape of CO_2 reduction (see "Enhanced sampling simulations" section). This procedure (MD enhanced sampling, collection of new configurations, DFT single-point calculation, and training) was iterated until reliable MLIPs capable of fully describing the CO_2 reduction to CO were obtained. The illustration of our workflow is depicted in Supplementary Fig. 1b.

Ultimately, we constructed two training sets for describing CO_2 reduction process at the Ag(111)/H_2O interface under PZC and CP conditions, comprised of 6449 and 5777 configurations, respectively. The composition of the two training sets is reported in Supplementary Fig. 30. 600 configurations along the reaction pathways and transition states were selected as test sets for evaluating the accuracy of forces predicted by the MLIPs under PZC and CP conditions, respectively (Supplementary Fig. 31).

The MLIPs for modeling the CO_2 adsorption process at the Ag(111) surface with a fully implicit solvent model at PZC and constant potentials of −1 V, −1.5 V, and −2 V vs. SHE were obtained using the same protocol but trained separately. The final training set for these four MLIPs consists of 911 configurations.

Molecular Dynamics Simulations

Classical molecular dynamics simulations were preformed with the Large-scale Atomic/Molecular Massively Parallel Simulator (LAMMPS) program[74], patched with MACE 0.3.4 and PLUMED 2.9[75]. NVT simulations were performed with an integration time step of 0.5 fs. The temperature was controlled using a stochastic velocity scaling thermostat[76] with a coupling constant of 50 fs.

During the active learning stage, simulations were performed with p(3×3) and p(4×4) Ag(111)/H_2O models. One interfacial water molecule would be substituted by CO_2 molecule when considering the

reaction of CO_2 to CO conversion. When the final MLIPs were obtained, a 5-layer p(6 × 6) Ag(111) slab containing 180 water molecules (the thickness of explicit water is around 20 Å and the density of water is 1 g/cm^3) was used for simulating properties of the Ag(111)/H_2O interface. The water density profiles in Fig. 2a confirm that the thickness of explicit water used in our simulation is sufficient to capture the transition from interfacial to bulk water properties. To evaluate the CO_2 reduction elementary reaction steps with OPES-biased simulation, a 5-layer p(5 × 5) Ag(111) slab with 119 water molecules and one CO_2 molecule was used, representing the reaction in a neutral electrolyte (pH = 7). In all simulations, the bottom two layers of the Ag slab were fixed to simulate bulk phase structure. The temperature was set to 330 K to better describe the geometrical properties of water at room temperature in all the simulations, as suggested in Supplementary Fig. 32. The use of MLIPs provided an approximately 10^5-fold speed-up over grand-canonical DFT calculations (Supplementary Table 7), allowing the extensive sampling required to capture slow interfacial dynamics and obtain statistically robust thermodynamic and kinetic insights.

Enhanced sampling simulations

The On-the-fly Probability Enhanced Sampling (OPES)[29,77], implemented in the open source PLUMED plugin, was used for exploring the reactive space and obtaining the free energy surfaces. Two types of collective variables (CVs) were employed during the OPES-biased simulations. One CV corresponds to the distance between two reactive intermediates or the vertical distance of the intermediate from the surface. The other CV represents the maximum coordination number, which captures the chemical bond formation and cleavage of critical components:

$$C.N._{\cdot \mathrm{A,B}} = \sum_{j \in \mathrm{B}}^{N_j} \frac{1 - \left(\frac{d_{ij}}{r_0}\right)^n}{1 - \left(\frac{d_{ij}}{r_0}\right)^m} \tag{3}$$

$$S_{\mathrm{AB}}^{\max} = \beta \log \sum_{i \in \mathrm{A}} \exp\left(\frac{C.N._{\cdot \mathrm{A,B}}}{\beta}\right) \tag{4}$$

Here, d_{ij} denotes the distance between atoms i of species A and atoms j of species B, and r_0 is the reference distance between the two species. The exponents n and m control the sharpness of the function, while β governs the smoothness of the soft maximum function, which is set to 0.05. A detailed application of the CVs and OPES barriers (ΔE) for each elementary step is provided in Supplementary Method 2 and Supplementary Figs. 33–36.

Data availability

Inputs and instructions to reproduce the results presented in this manuscript can be found in the Zenodo repository (https://doi.org/10.5281/zenodo.17212732). Source data are provided with this paper.

Code availability

The results presented in this manuscript were obtained using the commercial computational package VASP, as well as publicly available software packages, including LAMMPS, PLUMED, and MACE.

References

1. Birdja, Y. Y. et al. Advances and challenges in understanding the electrocatalytic conversion of carbon dioxide to fuels. *Nat. Energy* **4**, 732–745 (2019).
2. Chen, J. & Wang, L. Effects of the catalyst dynamic changes and influence of the reaction environment on the performance of electrochemical CO_2 reduction. *Adv. Mater.* **34**, 2103900 (2022).
3. Kibria, M. G. et al. Electrochemical CO_2 reduction into chemical feedstocks: from mechanistic electrocatalysis models to system design. *Adv. Mater.* **31**, 1807166 (2019).
4. Ma, H., Ibáñez-Alé, E., You, F., López, N. & Yeo, B. S. Electrochemical formation of C_{2+} products steered by bridge-bonded * CO confined by * OH domains. *J. Am. Chem. Soc.* **146**, 30183–30193 (2024).
5. Tian, X. et al. Efficient electroreduction of high-pressure gaseous and supercritical CO_2 to CO in a zero-gap electrolyzer. *ACS Sustain. Chem. Eng.* **13**, 10495–10503 (2025).
6. Xu, A., Govindarajan, N., Kastlunger, G., Vijay, S. & Chan, K. Theories for electrolyte effects in CO_2 electroreduction. *Acc. Chem. Res.* **55**, 495–503 (2022).
7. Zhou, Y., Ouyang, Y., Zhang, Y., Li, Q. & Wang, J. Machine learning assisted simulations of electrochemical interfaces: recent progress and challenges. *J. Phys. Chem. Lett.* **14**, 2308–2316 (2023).
8. Liu, L. & Xiao, H. Inverted region in electrochemical reduction of CO_2 induced by potential-dependent Pauli repulsion. *J. Am. Chem. Soc.* **145**, 14267–14275 (2023).
9. Le, J.-B., Yang, X.-H., Zhuang, Y.-B., Jia, M. & Cheng, J. Recent progress toward ab initio modeling of electrocatalysis. *J. Phys. Chem. Lett.* **12**, 8924–8931 (2021).
10. Le, J. B., Yang, X. H., Zhuang, Y. B., Jia, M. & Cheng, J. Recent progress toward ab initio modeling of electrocatalysis. *J. Phys. Chem. Lett.* **12**, 8924–8931 (2021).
11. Wang, J. et al. Spatially and temporally understanding dynamic solid-electrolyte interfaces in carbon dioxide electroreduction. *Chem. Soc. Rev.* **52**, 5013–5050 (2023).
12. Ringe, S. et al. Understanding cation effects in electrochemical CO_2 reduction. *Energy Environ. Sci.* **12**, 3001–3014 (2019).
13. Re Fiorentin, M. et al. Silver electrodes are highly selective for CO in CO_2 electroreduction due to interplay between voltage dependent kinetics and thermodynamics. *J. Phys. Chem. Lett.* **15**, 11538–11545 (2024).
14. Chen, L. D., Urushihara, M., Chan, K. & Nørskov, J. K. Electric field effects in electrochemical CO_2 reduction. *ACS Catal.* **6**, 7133–7139 (2016).
15. Le, J.-B., Fan, Q. -Y., Li, J.-Q. & Cheng, J. Molecular origin of negative component of Helmholz capacitance at electrified Pt (111)/water interface. *Sci. Adv.* **6**, eabb1219 (2020).
16. Li, C. et al. In situ probing electrified interfacial water structures at atomically flat surfaces. *Nat. Mater.* **18**, 697–701 (2019).
17. Jia, M., Zhuang, Y. B., Wang, F., Zhang, C. & Cheng, J. Water-mediated proton hopping mechanisms at the SnO_2 (110)/H_2O interface from ab initio deep potential molecular dynamics. *Precis. Chem.* **2**, 644–654 (2024).
18. Li, P. et al. Hydrogen bond network connectivity in the electric double layer dominates the kinetic pH effect in hydrogen electrocatalysis on Pt. *Nat. Catal.* **5**, 900–911 (2022).
19. Lian, Z., Dattila, F. & López, N. úria Stability and lifetime of diffusion-trapped oxygen in oxide-derived copper CO_2 reduction electrocatalysts. *Nat. Catal.* **7**, 401–411 (2024).
20. Zhang, Z. et al. Molecular understanding of the critical role of alkali metal cations in initiating CO_2 electroreduction on Cu(100) surface. *Nat. Commun.* **15**, 612 (2024).
21. Mathew, K., Kolluru, V. S., Mula, S., Steinmann, S. N. & Hennig, R. G. Implicit self-consistent electrolyte model in plane-wave density-functional theory. *J. Chem. Phys.* **151**, 234101 (2019).
22. Chan, K. & Nørskov, J. K. Potential DEPENDENCE OF ELECTROCHEMICAL BARRIERS FROM AB INITIO CALCulations. *J. Phys. Chem. Lett.* **7**, 1686–1690 (2016).
23. Yu, S., Levell, Z., Jiang, Z., Zhao, X. & Liu, Y. What is the rate-limiting step of oxygen reduction reaction on Fe–N–C catalysts? *J. Am. Chem. Soc.* **145**, 25352–25356 (2023).

24. Le, D. An explicit-implicit hybrid solvent model for grand canonical simulations of the electrochemical environment. Preprint at *ChemRxiv* https://doi.org/10.26434/chemrxiv-2023-z2n4n (2023).
25. Xia, Z. & Xiao, H. Grand canonical ensemble modeling of electrochemical interfaces made simple. *J. Chem. Theory Comput.* **19**, 5168–5175 (2023).
26. Behler, J. & Parrinello, M. Generalized neural-network representation of high-dimensional potential-energy surfaces. *Phys. Rev. Lett.* **98**, 146401 (2007).
27. Zhang, L., Han, J., Wang, H., Car, R. & E, W. Deep potential molecular dynamics: a scalable model with the accuracy of quantum mechanics. *Phys. Rev. Lett.* **120**, 143001 (2018).
28. Batatia, I., Kovacs, D. P., Simm, G., Ortner, C. & Csányi, G. ábor Mace: higher order equivariant message passing neural networks for fast and accurate force fields. *Adv. Neural Inf. Process. Syst.* **35**, 11423–11436 (2022).
29. Invernizzi, M. & Parrinello, M. Rethinking metadynamics: from bias potentials to probability distributions. *J. Phys. Chem. Lett.* **11**, 2731–2736 (2020).
30. Yang, M., Raucci, U. & Parrinello, M. Reactant-induced dynamics of lithium imide surfaces during the ammonia decomposition process. *Nat. Catal.* **6**, 829–836 (2023).
31. Tosello Gardini, A., Raucci, U. & Parrinello, M. Machine learning-driven molecular dynamics unveils a bulk phase transformation driving ammonia synthesis on barium hydride. *Nat. Commun.* **16**, 2475 (2025).
32. Bonati, L. et al. The role of dynamics in heterogeneous catalysis: surface diffusivity and N_2 decomposition on Fe(111). *Proc. Natl. Acad. Sci. USA* **120**, e2313023120 (2023).
33. Mambretti, F., Raucci, U., Yang, M. & Parrinello, M. How does structural disorder impact heterogeneous catalysts? The case of ammonia decomposition on non-stoichiometric lithium imide. *ACS Catal.* **14**, 1252–1256 (2024).
34. Zhang, P., Gardini, AxelTosello, Xu, X. & Parrinello, M. Intramolecular and water mediated tautomerism of solvated glycine. *J. Chem. Inf. Model.* **64**, 3599–3604 (2024).
35. Brookes, S. G. H., Kapil, V., Michaelides, A. & Schran, C. CO2 hydration at the air–water interface: A surface-mediated "in-and-out" mechanism, *Proc. Natl. Acad. Sci. USA* **122**, e2502684122 (2025).
36. Yang, M., Karmakar, T. & Parrinello, M. Liquid-liquid critical point in phosphorus. *Phys. Rev. Lett.* **127**, 080603 (2021).
37. Yang, X., Bhowmik, A., Vegge, T. & Hansen, H. A. Neural network potentials for accelerated metadynamics of oxygen reduction kinetics at Au-water interfaces. *Chem. Sci.* **14**, 3913–3922 (2023).
38. Rice, P. S., Liu, Z.-P. & Hu, P. Hydrogen coupling on platinum using artificial neural network potentials and DFT. *J. Phys. Chem. Lett.* **12**, 10637–10645 (2021).
39. Andrade, M. F. C., Ko, H.-Y., Zhang, L., Car, R. & Selloni, A. Free energy of proton transfer at the water-TiO_2 interface from ab initio deep potential molecular dynamics. *Chem. Sci.* **11**, 2335–2341 (2020).
40. Sun, M., Jin, B., Yang, X. & Xu, S. Probing nuclear quantum effects in electrocatalysis via a machine-learning enhanced grand canonical constant potential approach. *Nat. Commun.* **16**, 3600 (2025).
41. Hu, Z. Y., Luo, L. H., Shang, C. & Liu, Z. P. Free energy pathway exploration of catalytic formic acid decomposition on Pt-group metals in aqueous surroundings. *ACS Catal.* **14**, 7684–7695 (2024).
42. Endrődi, B. et al. Operando cathode activation with alkali metal cations for high current density operation of water-fed zero-gap carbon dioxide electrolysers. *Nat. Energy* **6**, 439–448 (2021).
43. Kuhl, K. P. et al. Electrocatalytic conversion of carbon dioxide to methane and methanol on transition metal surfaces. *J. Am. Chem. Soc.* **136**, 14107–14113 (2014).
44. Ma, M., Trześniewski, B. J., Xie, J. & Smith, W. A. Selective and efficient reduction of carbon dioxide to carbon monoxide on oxide-derived nanostructured silver electrocatalysts. *Angew. Chem.* **128**, 9900–9904 (2016).
45. Frumkin, A. N., Petrii, O. A. & Damaskin, B. B. Potentials of zero charge. In *Comprehensive Treatise of Electrochemistry: The Double Layer*. 221–289 (Springer, 1980).
46. Larson, N. R. et al. Conformational changes and drivers of monoclonal antibody liquid-liquid phase separation. *J. Pharm. Sci.* **112**, 680–690 (2023).
47. Ahmed, M., Namboodiri, V., Singh, A. K. & Mondal, J. A. On the intermolecular vibrational coupling, hydrogen bonding, and librational freedom of water in the hydration shell of mono-and bivalent anions. *J. Chem. Phys.* **141**, 164708 (2014).
48. Wang, Y.-H. et al. In situ Raman spectroscopy reveals the structure and dissociation of interfacial water. *Nature* **600**, 81–85 (2021).
49. Monteiro, M. C. O. et al. Absence of CO_2 electroreduction on copper, gold and silver electrodes without metal cations in solution. *Nat. Catal.* **4**, 654–662 (2021).
50. Qin, X., Vegge, T. & Hansen, HeineAnton Cation-coordinated inner-sphere CO_2 electroreduction at Au–water interfaces. *J. Am. Chem. Soc.* **145**, 1897–1905 (2023).
51. Alsunni, Y. A., Alherz, A. W. & Musgrave, C. B. Electrocatalytic reduction of CO_2 to CO over Ag(110) and Cu(211) modeled by grand-canonical density functional theory. *J. Phys. Chem. C.* **125**, 23773–23783 (2021).
52. Marx, D., Chandra, A. & Tuckerman, M. E. Aqueous basic solutions: hydroxide solvation, structural diffusion, and comparison to the hydrated proton. *Chem. Rev.* **110**, 2174–2216 (2010).
53. Rosen, J. et al. Mechanistic insights into the electrochemical reduction of CO_2 to CO on nanostructured Ag surfaces. *ACS Catal.* **5**, 4293–4299 (2015).
54. Zhang, X.-G., Jin, X., Wu, D.-Y. & Tian, Z.-Q. Selective electrocatalytic mechanism of CO_2 reduction reaction to CO on silver electrodes: a unique reaction intermediate. *J. Phys. Chem. C.* **122**, 25447–25455 (2018).
55. Chang, X. et al. C-C coupling is unlikely to be the rate-determining step in the formation of C_{2+} products in the copper-catalyzed electrochemical reduction of CO. *Angew. Chem. Int. Ed.* **61**, e202111167 (2022).
56. Schlögl, R. Heterogeneous catalysis. *Angew. Chem. Int. Ed.* **54**, 3465–3520 (2015).
57. Yuan, Y. et al. Water in electrocatalysis. *Angew. Chem. Int. Ed.* **64**, e202425590 (2025).
58. Waegele, M. M., Gunathunge, C. M., Li, J. & Li, X. How cations affect the electric double layer and the rates and selectivity of electrocatalytic processes. *J. Chem. Phys.* **151**, 160902 (2019).
59. Kresse, G. & Furthmüller, J. Efficient iterative schemes for ab initio total-energy calculations using a plane-wave basis set. *Phys. Rev. B* **54**, 11169 (1996).
60. Kresse, G. & Furthmüller, J. Efficiency of ab-initio total energy calculations for metals and semiconductors using a plane-wave basis set. *Comput. Mater. Sci.* **6**, 15–50 (1996).
61. Kresse, G. & Joubert, D. From ultrasoft pseudopotentials to the projector augmented-wave method. *Phys. Rev. B* **59**, 1758 (1999).
62. Blöchl, P. E. Projector augmented-wave method. *Phys. Rev. B* **50**, 17953 (1994).
63. Furness, J. W., Kaplan, A. D., Ning, J., Perdew, J. P. & Sun, J. Accurate and numerically efficient r^2SCAN meta-generalized gradient approximation. *J. Phys. Chem. Lett.* **11**, 8208–8215 (2020).
64. Ning, J. et al. Workhorse minimally empirical dispersion-corrected density functional with tests for weakly bound systems: r^2 SCAN+ rVV 10. *Phys. Rev. B* **106**, 075422 (2022).
65. Mathew, K., Sundararaman, R., Letchworth-Weaver, K., Arias, T. A. & Hennig, R. G. Implicit solvation model for density-functional study of nanocrystal surfaces and reaction pathways. *J. Chem. Phys.* **140**, 084106 (2014).

66. Cao, H., Lv, X., Qian, S., Li, J. & Wang, Yang-Gang Constant potential thermodynamic integration for obtaining the free energy profile of electrochemical reaction. *J. Phys. Chem. Lett.* **15**, 1314–1320 (2024).
67. Vavra, J. et al. Solution-based Cu+ transient species mediate the reconstruction of copper electrocatalysts for CO_2 reduction. *Nat. Catal.* **7**, 89–97 (2024).
68. Chen, L. et al. A constant potential reactor framework for electrochemical reaction simulations. Preprint at https://arxiv.org/abs/2411.16330 (2024).
69. Wang, R., Fang, S., Huang, Q. & Liu, Y. Constant-potential machine learning force field for the electrochemical interface. *J. Chem. Theory Comput.* **21**, 7628–7635 (2025).
70. Kovács, D., Batatia, I., Arany, E. & Csányi, G. Evaluation of the mace force field architecture: from medicinal chemistry to materials science. *J. Chem. Phys.* **159**, 044118 (2023).
71. Batatia, I. et al. The design space of E(3)-equivariant atom-centred interatomic potentials. *Nat. Mach. Intell.* **7**, 56–67 (2025).
72. Batatia, I. et al. A foundation model for atomistic materials chemistry. Preprint at https://arxiv.org/abs/2401.00096 (2023).
73. Raucci, U. Capturing excited state proton transfer dynamics with reactive machine learning potentials. *J. Phys. Chem. Lett.* **16**, 4900–4906 (2025).
74. Thompson, A. P. Lammps-a flexible simulation tool for particle-based materials modeling at the atomic, meso, and continuum scales. *Comput. Phys. Commun.* **271**, 108171 (2022).
75. Tribello, G. A., Bonomi, M., Branduardi, D., Camilloni, C. & Bussi, G. PLUMED 2: new feathers for an old bird. *Comput. Phys. Commun.* **185**, 604–613 (2014).
76. Bussi, G., Donadio, D. & Parrinello, M. Canonical sampling through velocity rescaling. *J. Chem. Phys.* **126**, 014101 (2007).
77. Invernizzi, M., Piaggi, P. M. & Parrinello, M. Unified approach to enhanced sampling. *Phys. Rev. X* **10**, 041034 (2020).
78. Turisini, M., Cestari, M. & Amati, G. Leonardo: a Pan-European pre-exascale supercomputer for HPC and AI applications. *J. Large Scale Res. Facil.* **9**, A186 (2024).
79. Marcos-Alcalde, I., Setoain, J., Mendieta-Moreno, J. I., Mendieta, J. & Gomez-Puertas, P. MEPSA: minimum energy pathway analysis for energy landscapes. *Bioinformatics* **31**, 3853–3855 (2015).

Acknowledgements

The authors would like to express their gratitude to Luigi Bonati, Jintu Zhang, Francesco Mambretti, Peilin Kang, and Michele Bianchi for helpful discussions. We acknowledge ISCRA for awarding projects access to the LEONARDO supercomputer (projects HP10B9XORR and HP10B3VEJJ)[78], owned by the EuroHPC Joint Undertaking, hosted by CINECA (Italy). We gratefully acknowledge the Data Science and Computation Facility and its Support Team for their support and assistance on the IIT High Performance Computing Infrastructure. X.T. and Y.Z. received support from the Fundamental Research Funds for the Central Universities (2022ZFJH04).

Author contributions

X.H., Y.Z., and M.P. supervised the project. X.T. and A.T.G. performed the simulations. X.T., A.T.G., and U.R. analyzed the data and wrote the manuscript. All authors discussed the results and contributed to the manuscript preparation.

Competing interests

The authors declare no competing interests.

Additional information

Supplementary information The online version contains supplementary material available at https://doi.org/10.1038/s41467-025-65630-1.

Correspondence and requests for materials should be addressed to Hai Xiao, Yuqun Zhuo or Michele Parrinello.

Peer review information *Nature Communications* thanks Zhen Zhou, Wen-Chuan Lai, and the other anonymous reviewer(s) for their contribution to the peer review of this work. A peer review file is available.